

# Metal Cluster Support Interactions in the Cu/ZnO System: A QM/MM Study

S. T. Bromley,<sup>†,‡</sup> S. A. French,<sup>†</sup> A. A. Sokol,<sup>†</sup> C. R. A. Catlow,<sup>\*,†</sup> and P. Sherwood<sup>§</sup>

*Davy-Faraday Research Laboratory, The Royal Institution of Great Britain, 21 Albemarle Street, London W1S 4BS, U.K., and CLRC, Daresbury Laboratory, Warrington WA4 4AD, U.K.*

*Received: October 30, 2002; In Final Form: February 25, 2003*

To study in detail the interaction of copper atoms and clusters in various, potentially important catalytic oxidation states (Cu, Cu<sup>+</sup>, and Cu<sup>2+</sup>) on polar surfaces, we have applied a hybrid QM/MM embedding model within the computational chemistry package ChemShell. Using the model, we study specific Cu/ZnO surface sites treated at a high *ab initio* level of theory while also maintaining the effects of steric bulk constraints, the influence of a long-range electrostatic field, and a self-consistent treatment of polarization of the ZnO support. The model has been applied to copper atoms, ions and clusters (Cu<sub>*n*</sub>, *n* = 1, 4) on the zinc-terminated (0001) surface of ZnO. The anchoring sites for copper adsorption have been identified as vacant zinc interstitial surface sites that result from the reconstruction of polar surfaces. The undercoordinated oxygens at these sites strongly bind to the copper anchor in all three oxidation states whereas the preferred path for cluster growth is shown to be by addition of neutral copper on both Cu<sup>0</sup> and Cu<sup>+</sup> species.

## 1. Introduction

The Cu/ZnO system is well established as the leading industrial catalyst for the synthesis of methanol. Despite over three decades of commercial use, many questions remain unresolved concerning the role, nature, and activity of the various oxidation states of copper in the catalyst. Numerous studies have attempted to resolve these issues by employing many different model systems and catalyst preparations. Unfortunately, although each of these studies often gives particular insights into the workings of the catalyst, the diversity of investigative approaches and the problems in accurate characterization of the final complex catalyst make the results of different studies difficult to compare and assess. This uncertainty has led to the various oxidation states of copper in Cu/ZnO based catalysts being linked to the catalytic activity by differing postulated mechanisms.

After synthesis of Cu/ZnO catalysts, clusters and seams of copper are found running throughout the ZnO matrix, which can be partially oxidized in various ways in different domains.<sup>1–3</sup> Thus Cu<sub>*x*</sub>O<sub>*y*</sub> clusters are formed with oxygen partially removed during the catalyst pretreatment (reduction in hydrogen under 40–100 kbar and at 200–300 °C). The preparation procedure leads to a spread in oxidation states in the working catalysts with relative populations dependent on thermodynamic and kinetic factors. It is further known that both Cu<sup>+</sup> and Cu<sup>2+</sup> ions formed in this preparation may both dissolve into and be stabilized within the bulk of ZnO.<sup>1,3–6</sup> The presence of these ions together with the neutral copper has been suggested as a way in which copper can affect the defect structure and thus the activity of the catalyst.<sup>2,3</sup>

Cu<sup>+</sup> and Cu<sup>2+</sup> ions can also be stabilized in exposed copper oxides and/or atomically dispersed on the ZnO surface.<sup>6–10</sup>

Although surface Cu<sup>2+</sup> species seem not to play an active chemical role in catalysis,<sup>6</sup> they are present in small amounts throughout the as prepared catalyst. Cu<sup>2+</sup>, and Cu<sup>+</sup>, species can also be formed from the oxidation of surface neutral copper via reaction with CO<sub>2</sub> during the methanol synthesis<sup>9</sup> reaction. Subsequently, such ions can penetrate into the ZnO bulk potentially affecting the structure and activity of both the support and the copper clusters.<sup>3,4</sup> In contrast to the relatively small number of Cu<sup>2+</sup> ions, numerous Cu<sup>+</sup> surface species are left by the preparative treatments of Cu/ZnO catalysts. The influence of Cu<sup>+</sup> species on the activity of the catalyst is thought by many to be far more direct and important.<sup>7–9,11</sup> Cu<sup>+</sup> on the surface of ZnO, for example, is known to be an active center for CO adsorption and activation.<sup>8,11</sup> It has also been advocated that the ratio of surface Cu<sup>+</sup> sites to neutral Cu sites on the surface determines the catalytic activity of the system.<sup>7,8</sup> In such a scenario, ZnO plays an active part in the formation of Cu<sup>+</sup> sites via migration of ZnO<sub>*x*</sub> species onto the surface and into the copper clusters.<sup>7,12</sup> Neutral copper alone is also often regarded to be the main active component in the Cu/ZnO catalyst. In this picture the ZnO bulk is treated simply as an inert support, with the copper metal exposed at the ZnO surface providing the sites for catalysis.<sup>13–16</sup> Other studies though strongly suggest that ZnO, compared to other supports such as SiO<sub>2</sub>, has a particularly strong influence on the chemical and physical properties of neutral copper.<sup>17</sup> This interaction is likely to form Zn–Cu alloy sites,<sup>9,18</sup> which have also been proposed as synergetic active catalytic centers.<sup>7,9,19</sup>

In addition to its proven catalytic importance, the system of Cu clusters interacting with ZnO is also relevant to sensor applications<sup>20</sup> and more generally as a model oxide-supported metal system.<sup>21,22</sup> Previous theoretical work on oxide-supported copper has tended to concentrate on the extended nonpolar defect-free surfaces of MgO using both periodic boundary conditions<sup>23</sup> and embedded cluster approaches<sup>24</sup> and also on small fragments of defect-free and defective silica.<sup>25</sup> In this paper we extend these investigations to the case of copper interacting

\* Corresponding author. E-mail: richard@ri.ac.uk.

<sup>†</sup> The Royal Institution of Great Britain.

<sup>‡</sup> Current address: Laboratory of Applied Organic Chemistry and Catalysis, DelftChemTech, Delft University of Technology, Julianalaan 136, 2628 BL Delft, The Netherlands.

<sup>§</sup> Daresbury Laboratory.

with polar oxide surfaces using a QM/MM embedding scheme allowing for self-consistent polarization of the QM-treated cluster and the MM-treated oxide support. Specifically, we examine the interaction of copper in various oxidation states with the zinc-terminated polar (0001) surface of the stable, catalytically relevant wurtzite phase of ZnO (zincite). Copper on the (0001)-Zn surface of ZnO has been well characterized by a number of experimental probes in surface science experiments<sup>26,27</sup> and has also been used in model catalyst studies,<sup>28</sup> as the polar surfaces of ZnO are themselves catalytically active.<sup>29,30</sup> From such studies it has been shown that at low coverages, highly dispersed neutral copper may assume a partial positive charge by its interaction with the surface, whereas at higher coverages neutral three-dimensional clusters are thermodynamically preferred.<sup>27</sup>

To explore the interaction of copper in the three oxidation states (Cu, Cu<sup>+</sup>, Cu<sup>2+</sup>) with the (0001)-Zn surface of ZnO, and also to study the influence of this interaction on the known, largely neutral copper clusters in the system, we first developed a detailed model of zincite, and its polar surfaces.<sup>31</sup> Copper atoms in these oxidation states were then introduced at the likely adsorption sites on our (0001)-Zn surface model, and on top of these sites neutral copper was further added to model the growth of copper clusters in the Cu/ZnO system. Our investigations are aimed at clarifying the nature of the Cu/ZnO interaction: how it is affected by and affects the oxidation state of the supported copper, and the relevance of such interactions in real systems.

## 2. Methodology

**2.1. Solid-State Embedding Technique.** One of the main difficulties in accurately modeling oxide-supported metals lies in providing an adequate treatment of the support itself. The problem is 2-fold: first, an accurate model of the support must be used, and second, enough of the support, or at least its effects, must be included in the model to account for the long-range interactions of the support (e.g., steric constraints and Madelung field). For zincite, both these problems are particularly relevant due to its ionic nature and the uncertainty regarding the structure of the (0001)-Zn surface. The former gives rise to long-range electrostatic fields, which have been shown to be very important in theoretical studies of molecules interacting with ionic oxide supports.<sup>32–36</sup> A good treatment of the electrostatics of the support is especially important when dealing with the adsorption of charged species (e.g., Cu ions) on polarizable media (e.g., zincite). An embedding approach is particularly well suited to treat such systems, wherein a relatively small part of the support is used and the long-range electrostatics dealt with by a surrounding array of point charges whose magnitudes and positions are optimized to mimic accurately the Madelung field of the crystal both in the bulk and at the surface. We further extend this methodology in a newly developed hybrid quantum mechanical/molecular mechanical (QM/MM) multiregion embedding approach, as illustrated in Figure 1.

The physical system we wish to describe, in the ideal case, consists of a 2-dimensional semi-infinite support, whose periodic translational and local point group symmetry is broken by the presence of an adsorbate. As we are primarily concerned with processes of charge transfer bond making and breaking, a high-level QM description is essential for their accurate treatment.

A full QM treatment of an infinite system including long-range Coulombic interactions, however, is only possible using periodic boundary conditions. Assuming an artificially imposed periodicity, a fully QM supercell approach can be employed.

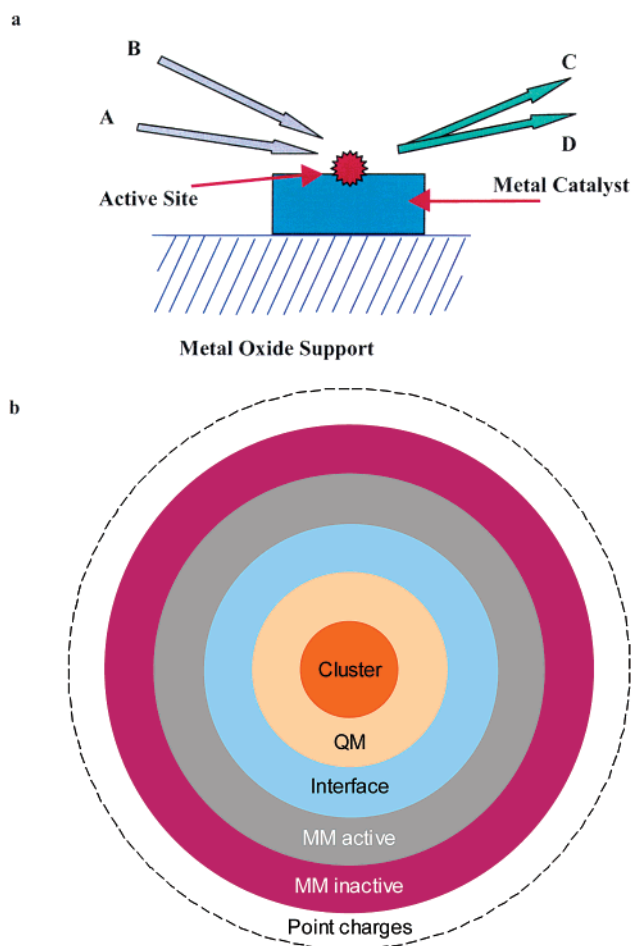


**Figure 1.** (a) Schematic of surface adsorption processes. (b) Embedding model: multiregion solution.

This technique is currently limited to small charge-neutral surface supercells (typically 100 atoms for ionic surface systems).<sup>37</sup> Thus the supercell approach neglects long-range polarization effects and introduces highly concentrated adsorbate–adsorbate interactions.

In contrast, relatively simple MM-based methods using polarizable ions have traditionally been very successful in their accurate description of both perfect periodic and defective polar solids and surfaces.<sup>38–40</sup> The response of most of the support to the presence of the adsorbate can thus be expected to be well reproduced by such methods. Based on this idea, our model first treats a small part of the support (together with any adsorbates) at a high QM level, region I, with the remainder of the system incorporated using MM polarizable ions, region II. The two regions are directly linked via an interface employing customized pseudopotentials on ZnO ions surrounding the QM region adding no extra atoms to the system (cf. link-atom embedding approaches widely used for covalent systems<sup>41–43</sup>).

Both QM and MM regions interact via direct short-range forces, with the QM atoms able to relax together with their closest neighbor MM ions. The QM and MM regions also self-consistently respond to longer range polarization effects; the QM region responds electronically to the field of the ZnO ionic matrix, and the MM region responds via the shell model to the field generated by the charge distribution of the QM region. The long-range steric bulk constraint of the crystal is taken into account by fixing a subset of MM atoms furthest from the QM centers. The long-range Madelung field is reproduced by the

field of the MM ions together with the set of point charges surrounding the whole system.

$$E^{\text{total}} = E^{\text{QM}} + E^{\text{MM}} \quad (1)$$

$$E^{\text{QM}} = \langle \Psi | \hat{H}^{\text{QM}} + \hat{V}^{\text{short}} + \hat{V}^{\text{long}} | \Psi \rangle + U_{\text{NN}} + U_{\text{N}}^{\text{long}} \quad (2)$$

$$E^{\text{MM}} = E^{\text{on-site}} + E^{\text{2-body}} + E^{\text{3-body}} + \dots \quad (3)$$

The QM energy term,  $E^{\text{QM}}$ , is constructed from (i) the expectation value of the usual many electron Hamiltonian of the QM region,  $\hat{H}^{\text{QM}}$ , together with contributions from the short-range potential,  $\hat{V}^{\text{short}}$ , of the immediate environment and the long-range Coulombic potential,  $\hat{V}^{\text{long}}$ , of the crystal remainder, and (ii) the Coulombic potential energy contribution of the QM nuclei in the field of each other,  $U_{\text{NN}}$ , and that of all MM centers,  $U_{\text{N}}^{\text{long}}$ . The MM energy term,  $E^{\text{MM}}$ , is simply the sum over all classical interactions within the MM region. Importantly, the total energy expression can be partitioned into respective QM and MM self-energy terms and a QM/MM interaction energy. This latter term is

$$U^{\text{embedding}}(R^{\text{QM}}, R^{\text{MM}}) \equiv \langle \Psi | \hat{V}^{\text{short}} + \hat{V}^{\text{long}} | \Psi \rangle + U_{\text{N}}^{\text{long}} \equiv U^{\text{polarizing}}(R^{\text{QM}}, R^{\text{MM}}) \quad (4)$$

and serves both as an embedding and polarizing potential energy. The forces on polarizable ions in the MM region from the QM region are obtained from the derivatives of  $E^{\text{total}}$  at each MM center with respect to their positions. Correspondingly, the forces on QM nuclei from the influence of the MM centers are calculated from the derivatives of  $E^{\text{total}}$  at each QM nucleus with respect to its position. The electronic state of the QM region self-consistently relaxes in the field of the embedding potential along with the field due to the updated QM nuclear positions.

The interactions across the interface between the QM and MM regions are taken into account in expression (4) by cation-centered semilocal large core pseudopotentials. These pseudopotentials provide a natural means by which the electrons can be confined to the QM region. For our purposes, pseudopotentials of the Hay–Wadt<sup>44</sup> form with a standard Stuttgart–Dresden parametrization were found to work effectively.<sup>45</sup>

In our description of the MM region, we have employed recently derived interatomic potentials that accurately model the zincite bulk and surface structures.<sup>40</sup> These potentials have proved to be very good in their reproduction of the bulk properties of zincite and in studies of both perfect and defective nonpolar surfaces. The potentials are based on the polarizable shell model due to Dick and Overhauser<sup>46</sup> and have a two-body form.

The model described has been implemented in the computational chemistry software environment ChemShell<sup>47</sup> based on the Tcl programming language. The MM contributions to the energy and forces in this implementation are computed using the GULP package<sup>48</sup> whereas for the QM part we used the GAMESS-UK code.<sup>49</sup>

**2.2. Surface Model.** Zinc oxide adopts a hexagonal, wurtzite structure ( $P6_3mc$  space group) under a wide range of pressures and temperatures including catalytically relevant working conditions and is present in nature as the mineral zincite. In the bulk, both zinc and oxygen ions are tetrahedrally coordinated and arranged in stacks of identical planes in the order ABAB, perpendicular to axis  $c$ . The local symmetry for each ion is determined by the lattice symmetry as  $C_{3v}$ . An ionic model of zincite based on formal charges for rigid zinc and polarizable oxygen ions has been developed and successfully applied in a

number of molecular mechanics studies.<sup>40,50–52</sup> This ionic atomistic model highlights the problem of surface polarity. In particular, on cleavage of the crystal along the A or B planes, two opposing polar surfaces are formed with an excess of Zn cations at the (0001) surface and an excess of O anions at the (000 $\bar{1}$ ) surface. This charge separation results in a dipole throughout the crystal, proportional to the thickness of the sample, leading to an energetically unstable electric field. Such a dipole is physically unsustainable in macroscopic samples, and thus a simple bulk termination of the zincite crystal proves to be physically impossible. Nevertheless, experiment shows that both zinc and oxygen terminated polar surfaces of ZnO are stable.<sup>29</sup> Potential mechanisms for dipole quenching in ionic materials have been postulated by Tasker<sup>53</sup> and recently reviewed by Noguera.<sup>54</sup> The key to all these mechanisms is a removal, or compensation, of the excess surface charge, which can be accomplished by ionic reconstruction, electron transfer between the two surfaces, or adsorption of charged moieties, e.g., in an electrolyte. In a recent X-ray diffraction work, a model of the (0001)-Zn surface with a 0.74 occupancy of surface Zn sites (i.e., 26% of Zn surface vacancies) together with surface relaxation was found to give the best fit to the experimental data.<sup>55</sup>

Direct visualization at near atomic resolution of the zinc terminated surface has been achieved by Dulub et al.<sup>56</sup> in their experimental work using surface tunneling microscopy. The authors have reported equilateral triangular islands and depressions of various sizes with further numerous small pits of unresolved structure. The fraction of zinc atoms missing from the surface was found to be close to that reported by Jedrecy et al.<sup>55</sup> Complementary evidence has been obtained for the oxygen terminated surface, which reports surface reconstruction albeit of a less defined nature.<sup>57</sup> Finally, vibrational spectroscopies provide strong evidence for the high concentration of three coordinated zinc vacant sites at ZnO surfaces; using this information, we were able to explain the main spectroscopic features of hydrogen adsorbed over ZnO, as summarized in ref 58.

Thus we conclude that zincite crystals simply maintain this fractional Zn occupancy (e.g., during crystal growth or cleavage) on the (0001)-Zn surface to avoid the energetic cost of the accumulation of a dipole across the crystal. In this work, we employ this model of partial Zn surface occupancy together with full surface relaxation throughout.

The Zn terminated surface in our semiclassical model is stabilized on removal of six Zn ions from a  $5 \times 5$  surface supercell, which yields a 0.76 occupancy of surface zinc sites. The vacant sites were positioned at maximum separation from each other. Two main kinds of surface sites result from the reconstruction: bulk terminated islands and vacancies, as shown in Figure 2.

The vacant zinc interstitial surface sites (VZISS) should not be seen as defects on the surface but are representative of the way in which the crystal rids itself of the large macroscopic dipole throughout the sample. These sites present natural traps to atomic and ionic species due to their morphology and the relatively low coordination of the surface oxygen atoms surrounding the VZISS (three zinc neighbors compared to four zinc neighbors on the bulk-terminated surface regions) and were therefore taken as primary adsorption sites for copper. In previous studies, we have successfully used similar interstitial surface sites, for the adsorption of hydrogen and intermediates in methanol synthesis, on the (0001)-Zn and (000 $\bar{1}$ )-O polar surfaces of ZnO.<sup>31,58</sup>



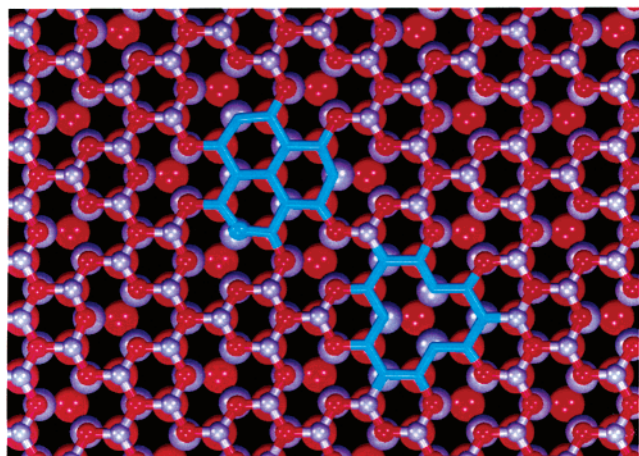


**Figure 2.** Structural model of the reconstructed (0001)-Zn surface of zincite obtained on MM relaxation. Two major surface features, bulk like island and vacant interstitial surface sites in the topmost terminating layer are highlighted. Oxygen: red/dark gray. Zinc: light gray.

**2.3. Embedding Model.** A two-dimensional periodic slab model of the two complementary reconstructed polar surfaces was fully relaxed using the MM methodology employing the computer code MARVIN.<sup>59</sup> To define our structural model, a hemispherical cut of the surface was made at a 25 Å radius from the VZISS. The atoms in the central core of this hemisphere (radius 13 Å, 426 atoms) were allowed to relax fully in all calculations with the remaining peripheral atoms (ca. 3750 cores and shells) fixed at their optimized positions from the MARVIN procedure. The thickness of the peripheral region was fixed at the cutoff radius of the short-range MM potentials. ChemShell was used to calculate the electrostatic potential due to the ZnO remainder throughout the core region, which was reproduced by a set of 125 point charges positioned around the hemisphere to within  $10^{-4}$  V. The VZISS is modeled as an embedded 13-atom QM cluster with a surrounding interface of 33 zinc based pseudopotentials and classical oxygen anions that corresponds to a 4 Å cutoff from the QM atoms. The classical representation of the nearest neighbor interaction between the QM region and the oxygen sublattice was found to be robust and effective in this study. A further refinement of the model, including oxygen based pseudopotentials, is underway.

The reported binding energies are given with respect to the sum of the energies of the bare (0001)-Zn surface and the free-space neutral copper cluster/atom. For the ionic copper species the reference state is also taken to be the corresponding free-space charged cluster. Although the QM/MM model presented thus far includes the influence of the long-range electrostatic field of the crystal on the QM center, in the case of a charged QM center the Hamiltonian explicitly includes the reciprocal polarization energy of the lattice induced by a charged center only over a finite number of sites in the crystal (up to the boundary of region II,  $r = R$ ). For charged QM centers, a correction term is therefore employed to account for the long-range polarization energy of the crystal by representing the charged center by a point charge,  $q$ , and considering the whole crystal with a defect as a dielectric of static permittivity  $\epsilon$  (taken to be that of ZnO). By integrating the electrostatic energy over the exterior of a sphere from  $R$  to infinity with the point charge at the center we obtain the polarization energy correction  $W_p$ ,

$$W_p = -\frac{q^2 \epsilon - 1}{2R \epsilon + 1} \quad (5)$$

Throughout, the value of  $R$  is 13 Å, and  $\epsilon$  is taken to be 9.78

**TABLE 1: Calculated Cu Dimer Properties for a Range of Basis Sets and Functionals, the Abbreviations Are Explained in the Text<sup>a</sup>**

	VTZ	VTZ-2pd	TZV	TZV-2pd	19s13p9d	$\Delta$
	VWN					
$d$ , Å	2.131	2.172	2.221	2.186	2.186	-0.034
$E_{\text{diss}}$ , eV	3.149	2.710	2.413	2.658	2.583	+0.65
$\nu$ , cm <sup>-1</sup>	320.1	299.6	270.7	289.1	285.1	+24.1
	B3LYP					
$d$ , Å	2.222	2.262	2.312	2.280	2.281	+0.06
$E_{\text{diss}}$ , eV	2.230	1.893	1.683	1.854	1.805	-0.226
$\nu$ , cm <sup>-1</sup>	270.9	255.9	235.3	248.0	244.3	-18.0
	B97-1					
$d$ , Å	2.232	2.275	2.326	2.296	2.298	+0.076
$E_{\text{diss}}$ , eV	2.431	2.152	1.905	2.092	2.082	+0.012
$\nu$ , cm <sup>-1</sup>	259.6	248.9	235.8	239.2	235.4	-25.8
	B97-1 (High Grid)					
$d$ , Å	2.232	2.275	2.326	2.296	2.298	+0.076
$E_{\text{diss}}$ , eV	2.431	2.153	1.905	2.092	2.083	+0.012
$\nu$ , cm <sup>-1</sup>	265.5	252.0	232.5	245.0	241.0	-20.0

<sup>a</sup> The experimental values are 2.22 Å for the bond length,  $d$ , 2.08 eV for the dissociation energy,  $E_{\text{diss}}$ , and 265 cm<sup>-1</sup> for the vibrational frequency,  $\nu$ .<sup>67</sup>  $\Delta$  is the difference between TZV-2pd and experimental data. All calculations employed the medium integration grid unless stated otherwise.

(one-third of the trace of the permittivity tensor) derived from our bulk semiclassical calculations, which can be compared with experimental values of 9.26 and 11.0.<sup>60</sup> All quoted cluster-surface binding energies incorporate this polarization correction, which for singly charged centers is found to be -0.45 eV, and for doubly charged centers -1.80 eV.

Equation 5 allows us to estimate the effect of embedding on calculated binding and ionization energies of charged species. Typically we consider molecular clusters of approximately 10 Å in diameter, which results in polarization energies of 1.2 eV for singly charged and 4.7 eV for doubly charged species. These significant energies are not accounted for by pure molecular cluster approaches but play an essential part in the stabilization of charged clusters on dielectric supports.

Graphical analyses of the spin and charge densities resulting from the embedded calculations along with numerical integration are used to assess the nature of the electronic states of the adsorbed copper. This method is preferred over using partitioning schemes such as Mulliken analysis, which is notoriously basis set dependent and relies on an arbitrary, and thus often unphysical, separation of atomic densities, a deficiency also found in the present study.

**2.4. Free-Space Copper Clusters.** As a preliminary test of our QM methodology, a series of calculations were performed on small free-space copper clusters.

Our choice of basis set and density functional for the embedded copper investigations was based on comparison of the calculated geometries, atomization energies, and harmonic frequencies of free-space copper dimer, trimer, and tetramer species with experimental data and high level ab initio calculations. Such small clusters proved to be particularly sensitive to the choice of calculation parameters and thus were an ideal test set. The results of these calculations, employing three different density functionals (VWN, B3LYP, and B97-1) together with a range of basis sets are shown in Table 1. The VWN functional used is a combination of a local density approximation (LDA) exchange term, in the Dirac form, together with the Vosko-Wilk-Nusair (VWN) correlation term.<sup>61</sup> B3LYP is the three parameter hybrid exchange-correlation functional due to Becke.<sup>62</sup> B97-1 is the Becke<sup>-97</sup> hybrid exchange-correlation functional<sup>63</sup>

**TABLE 2: Calculated Free-Space Copper Cluster ( $\text{Cu}_n$ ,  $n = 2-4$ ) Energies and Geometries Using the B97-1 Functional, High Grid, and the TZV-2pd Basis Set<sup>a</sup>**

	configuration	total energy (Ha)	$r_1$ (Å)	$r_2$ (Å)	$\theta$ (deg)
$\text{Cu}_2$	linear	-3280.85504	2.296		
$M = 1$			(2.27) <sup>†</sup>		
$\text{Cu}_2^+$	linear	-3280.57088	2.453		
$M = 2$			(2.36) <sup>†</sup>		
$\text{Cu}_2^{2+}$	(unstable)				
$\text{Cu}_3$	obtuse	-4921.28405	2.347	2.663	69.1
$M = 2$			(2.33)*, (2.35) <sup>†</sup>	(2.49)*, (2.58) <sup>†</sup>	(64.5)*, (66.6) <sup>†</sup>
	acute	-4921.28307	2.488	2.308	55.3
			(2.41)*, (2.47) <sup>†</sup>	(2.31)*, (2.31) <sup>†</sup>	(57.2)*, (55.8) <sup>†</sup>
$\text{Cu}_3^+$	equilateral	-4921.08095	2.416	2.418	60.1
$M = 1$			(2.38) <sup>†</sup>	(2.38) <sup>†</sup>	(60.0) <sup>†</sup>
$\text{Cu}_3^{2+}$	acute	-4920.57016	2.730	2.699	59.3
$M = 2$	obtuse	-4920.57001	2.689	2.846	63.9
$\text{Cu}_4$	planar	-6561.76191	2.458	2.323	56.4
$M = 1$			(2.45) <sup>†</sup>	(2.34) <sup>†</sup>	(57.0) <sup>†</sup>
	tetrahedral	-6561.70951	2.616	2.353	63.3; 53.5; 60.0
			(2.46) <sup>†</sup>	(2.46) <sup>†</sup>	(60.0) <sup>†</sup>
$\text{Cu}_4^+$	planar	-6561.52495	2.473	2.377	57.45
$M = 2$			(2.43) <sup>†</sup>	(2.39) <sup>†</sup>	(59.0) <sup>†</sup>
	tetrahedral	-6561.50898	2.570	2.410	62.0; 55.9; 60.0
$\text{Cu}_4^{2+}$	tetrahedral	-6561.12300	2.523	2.518	60.1; 59.9; 60.0
$M = 1$					

<sup>a</sup> For the  $\text{Cu}_3$  triangular clusters  $r_1$  denotes the length of the two equal edges and  $r_2$  the other edge. For the  $\text{Cu}_4$  planar rhomboidal clusters,  $r_1$  gives the length of the shortest diagonal and  $r_2$  the length of the other equal edges.  $\theta$  is the smallest angle between two  $r_2$  edges, for the tetrahedral clusters all internal angles are given. Geometries are compared with literature calculations in parentheses where available: \*configuration interaction calculations,<sup>70</sup> †GGA calculations.<sup>69</sup>  $M$  indicates multiplicity.

as re-parametrized by Hamprecht et al.<sup>64</sup> The basis sets are labeled as (i) VTZ (valence triple zeta basis set due to Ahlrichs<sup>65</sup>), (ii) VTZ-2pd (Ahlrichs VTZ with optimized polarization functions), (iii) TZV (triple zeta valence basis set due to Ahlrichs<sup>66</sup>), (iv) TZV-2pd (Ahlrichs TZV with optimized polarization functions), and (v) 19s13p9d (uncontracted basis set based on the Ahlrichs TZV basis set complemented by extra contracted functions and diffuse functions with zeta scaled by a factor of 3).

If we consider the Cu dimer bond length and employ the local functional, VWN, we find a gradual increase toward the experimental value of 2.22 Å<sup>67</sup> on improving the quality of the basis set from VTZ to TZV, as shown in Table 1. In contrast, the hybrid functionals together with the same change in basis set show an increase in Cu–Cu bond length, shifting away from the experimentally determined value. The addition of polarization functions to the TZV basis set shows, however, that the predicted Cu dimer bond length using the VWN functional worsens whereas the same increase in basis set quality for the hybrid functionals results in a better Cu–Cu geometry with respect to experiment; see Table 1. A further increase of the basis set to a fully uncontracted basis set with extra diffuse functions, 19s13p9d, shows no significant change for any functional employed, showing that the TZV-2pd basis set is relatively saturated. The poor performance of LDA is highlighted by the dissociation energies, which show a large overbinding tendency (>0.5 eV) for all basis sets employed, with respect to the experimental value. In contrast, the hybrid functionals perform well with B97-1, in particular, showing a good match with experiment (within 0.02 eV). For the harmonic frequencies, the VWN calculations show a small overestimation, and the hybrid functionals a small underestimation of the experimental value by a similar amount. Both the calculated dissociation energies and frequencies, as with the bond lengths, show no significant change when going from TZV-2pd to the fully uncontracted basis set.

Comparing the performance of the two hybrid functionals, we see little difference in the predictions for the geometry and

frequencies, with B3LYP showing a very small advantage, but a significant difference in the predicted dissociation energies, and with B97-1 showing a much better match with the experimental value.

The use of hybrid<sup>68</sup> and gradient-corrected functionals<sup>69</sup> has been shown previously, as in this work, to overestimate copper cluster bond lengths. It has further been advocated, as a pragmatic calculation strategy, that one use LDA-based functionals for obtaining good geometries, followed by gradient corrected or hybrid functional based single point calculations using the LDA-geometry to obtain more accurate energies.<sup>69</sup>

For our embedding model, however, we have to consider both the cluster and the support; although the geometry of free-space copper clusters is well reproduced by LDA, the support requires a better quality functional, with B3LYP and B97-1 being particularly effective. This feature is important when considering a cluster's interaction with an extended polarizable environment and potentially (as planned in future studies) adsorbates. Although our approach, using the B97-1 functional along with the TZV-2pd basis set, slightly overestimates the  $\text{Cu}_2$  bond length, as also found for high level modified coupled pair functional<sup>70</sup> and gradient corrected density functional calculations,<sup>69</sup> we note that our choice of functional and basis set yields excellent agreement with experiment for frequencies and, crucially, dissociation energies. Furthermore, a small contraction of the dimer bond has been attributed in the literature to relativistic effects,<sup>69</sup> which has been confirmed by our ZORA HF and ZORA MP2 calculations.<sup>71</sup>

The B97-1 functional and the TZV-2pd basis set, with a medium integration grid, was therefore used throughout our embedding investigations. The structural parameters of the optimized free-space  $\text{Cu}_3$  and  $\text{Cu}_4$  clusters for different charge states, using this methodology are shown in Table 2. The results are seen to compare well with other high level DFT and configuration interaction calculations, further confirming our choice of functional and basis set.

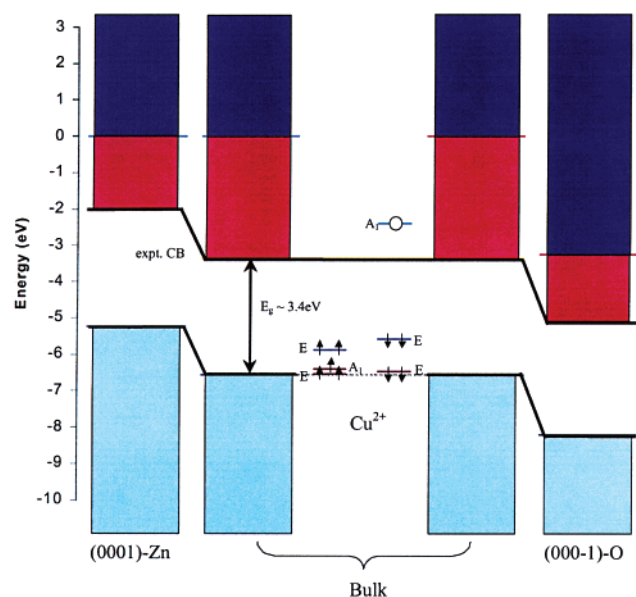


**Figure 3.** One-electron band structure of ZnO showing surface band bending and the bulk Cu impurity levels as calculated using the embedded cluster approach. Dark blue: conduction band (CB) as calculated by the current embedding method. Red: conduction band from experiment. Light blue: valence band (VB) as calculated by the current embedding method.

### 3. Electronic Structure and Geometry of Copper Adsorbates

We start our analyses with single copper atoms absorbed in the VZISS in three different oxidation states (0, 1+, 2+). We propose copper stabilized in the VZISS as anchoring sites for the formation of larger aggregates of copper atoms. Upon these copper-filled sites further neutral copper is then added to form supported  $\text{Cu}_n$  ( $n = 2-4$ ) clusters. Neutral copper atoms added to a copper ion in the VZISS may be regarded as forming singly and doubly charged supported clusters or potentially as neutral copper clusters interacting with a localized electron deficient surface site. The resultant species depend on the self-consistent solution of the most favorable electronic and nuclear configuration within the hybrid QM/MM scheme and is not specified prior to the calculation.

The site we have considered for copper adsorption is the vacant zinc interstitial surface site, which has a local  $C_{3v}$  symmetry about an axis through its center perpendicular to the plane of the ZnO surface. At longer distances, this local symmetry is broken by the structure of the reconstructed surface, which possesses both VZISS centers and bulk-terminated island sites (see Figure 2). Due to the arrangement of VZISS and island sites on the surface, an overall  $C_s$  symmetry results. The reflection plane passes through the center of the VZISS and one of its three undercoordinated oxygen atoms perpendicular to the plane of the surface.

To estimate the likely ground state of adsorbed copper and the possibility of electron transfer between the cluster and the surface, we consider the highest occupied and the lowest unoccupied states (HOMO and LUMO) of the bare ZnO surface and of the surface together with adsorbed copper. Significant relaxation processes in the surface layers at both zinc and oxygen terminated polar surfaces result in collinear dipole moments and associated surface band bending. The results are illustrated in Figure 3, in which we use our calculated one-electron Kohn–Sham energies to indicate relative positions of valence and conduction bands at the two polar surfaces and in the bulk.<sup>80</sup>

The HOMO of the bare (0001)-Zn surface is considered to represent the top of the surface valence band, and the LUMO to represent the bottom of the surface conduction band, with the vacuum level at zero. The (0001)-Zn surface band gap according to this approach is between 5.89 eV, at the bulk-terminated sites, and 6.70 eV at the VZISS sites; see Figure 3. By the nature of the DFT approach used in our methodology the most reliable description is provided for the occupied states and, possibly, localized unoccupied states. The conduction states in ZnO consist of oxygen 3s and zinc 4s and 4p contributions and are strongly delocalized, but they are constrained by the embedding potential in our model. The resulting kinetic energy is thus significantly overestimated, which contributes to a widening of the band gap. In contrast, the valence band is largely formed by the oxygen 2p states, which are localized and therefore we can have confidence in DFT to reproduce correctly this feature. In this paper we deal with electron-transfer processes from the valence band to well localized acceptor copper states and avoid using absolute positions of calculated conduction bands; hence we expect that errors associated with the overestimation of the band gap are small. In Figure 3 we show the position of the conduction band, defined by adding the experimental value for the band gap of 3.37 eV to the valence band.

Even though vacant interstitial surface sites are not true surface defects there is an important structural similarity between the two types of sites. Owing to the high coordination by surface ions, a large electrostatic potential of  $-10.05$  V is generated at the VZISS, which stabilizes positively charged adsorbates and should be compared to  $-23.91$  V for cation sites in the bulk of ZnO, where copper is known to assume a  $\text{Cu}^{2+}$  electronic state.<sup>1,3,6,72,73</sup> Both donor and acceptor levels of copper impurities ( $\text{Cu}^{2+}$ ) in the bulk lie in the band gap. The positive shift in the electrostatic potential when going from the bulk to the VZISS of 13.86 V should strongly stabilize one electron states localized on the VZISS with the effect on the acceptor band being of particular interest. We would therefore expect charge transfer from the valence band to a  $\text{Cu}^{2+}$  species trapped in the VZISS. On the other hand, in a vacuum, copper is a neutral (or even a negatively charged) species; on adsorption, the donor levels of neutral copper are significantly destabilized and an electron may be lost to the surface conduction bands or any available electron traps.

We now turn to the results of embedded cluster calculations to substantiate this qualitative analysis.

**3.1. Adsorbed Copper Atoms and Ions.** Atomic copper has an open shell  $(3d)^{10}(4s)^1$  electronic configuration and thus introduces spin density into the VZISS. Upon adsorption in the VZISS, the spin is localized in the diffuse 4s orbital of the free copper atom; this open shell state overlaps with states on the neighboring undercoordinated oxygen atoms.

Singly ionized copper atoms have a closed shell  $(3d)^{10}$  electronic configuration and are thus expected to interact weakly with the VZISS through electronic degrees of freedom. The spin and charge density for the adsorbed state show no spin density and no sign of charge transfer, but pronounced polarization of the three neighboring undercoordinated oxygen atoms by the copper ion.

The adsorption of the  $\text{Cu}^{2+}$  ion, as with the copper atom again entails spin being introduced into the Cu/ZnO system. For the  $\text{Cu}^{2+}$  ion, however, the open d-shell electronic configuration  $(3d)^9$  allows for potentially more complex states. First, as the d-electrons tend to be furthest from the surrounding maxima of charge density, i.e., that residing in the plane of the surface on



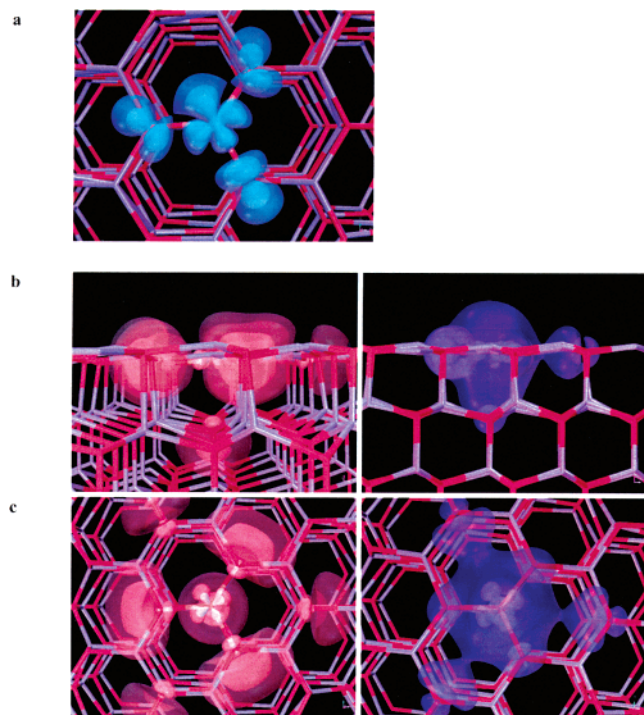


**Figure 4.** The spin density plot is shown in (a). Deformation density isosurface plots, (b) side view and (c) top view, for the  $\text{Cu}^{2+}$  adsorbate. Basins with excess charge density correspond to an electron component of an  $(e^-, h^+)$  complex and are shown on the left; basins with an electron deficit corresponding to the hole are shown on the right.

the undercoordinated oxygen sites of the VZISS, copper orbitals with lobes out of the plane ( $3d_{z^2}$ ,  $3d_{xz}$ ,  $3d_{yz}$ ) are preferentially occupied. (The  $z$ -axis is chosen to coincide with the surface normal). In the surface plane comprising the oxygen atoms two equivalent orbitals remain ( $3d_{x^2-y^2}$ ,  $3d_{xy}$ ). Of these two orbitals the one occupied has its lobes pointing between the electron maxima on the oxygen centers, reducing the overlap of occupied orbitals and therefore the electron–electron repulsion. The final orbital has lobes lying along the Cu–O bonds where the hole resides, reducing the negative charge density and thus reducing the repulsive energy, which accounts for the essential features of the observed spin distribution on an adsorbed  $\text{Cu}^{2+}$  ion in the VZISS, as shown in Figure 4a. Analyzing the spin density in more detail shows that indeed the spin, associated with the hole, is localized in a  $d_{x^2-y^2}$ -like orbital around the copper center (ca. 0.73e) and also on  $sp^3$ -like orbitals around the three closest oxygen centers (ca. 0.08e each).

Further analysis of the charge density for adsorbed  $\text{Cu}^{2+}$  reveals an unexpected effect: electron transfer occurs from the surface to a hybrid state consisting of the copper 4s orbital and the atomic orbitals of the neighboring oxygen atoms (see Figure 4b). The combination of copper and oxygen states makes it difficult to assign an exact amount of charge transferred to the Cu ion, but it can be estimated, by integration of the deformation density, to be between 0.5 and 1e. The resulting hole from this electron transfer is delocalized over nearest oxygen neighbors of the Cu ion and originates from the shared valence density, partially accounted for by states attributable to the nearest Zn ions. This hole covalently pairs to the 4s-like electron localized around the copper center. The reason that charge transfer occurs is the deep lying nature of the HOMO of  $\text{Cu}^{2+}$ , resulting in an electron transition from the valence band, stabilizing the complex ( $\text{Cu}^+$ ,  $h^+$ ). Even after charge transfer has occurred, the acceptor levels of the adsorbate are still below the top of

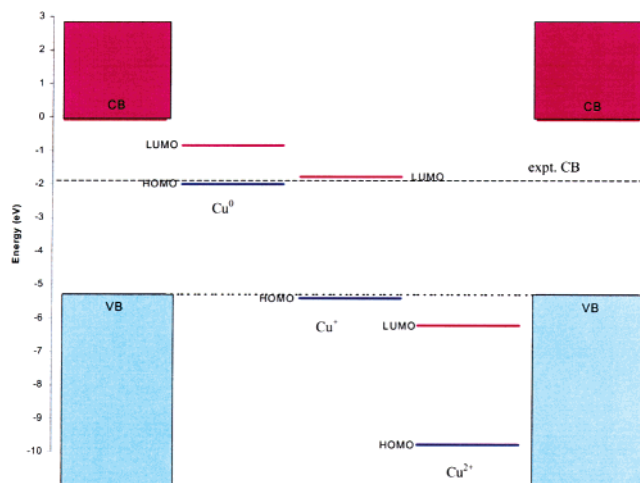


**Figure 5.** One-electron levels of copper adsorbate on the Zn terminated (0001) surface of ZnO as calculated by the current embedding method.

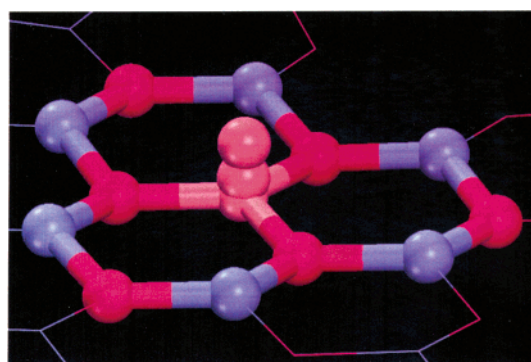


**Figure 6.** Cu atom adsorbate in the VZISS in three main oxidation states: 0, 1+, and 2+.

the valence band as shown in Figure 5, which suggests a possibility for further complex formation.

Thus, our calculations show that the electron component of the  $(\text{Cu}^+, h^+)$  complex is a hybrid between Cu 4s and valence band states, the latter being localized outside the first coordination sphere of the copper adsorbate. This model is in contrast to an intermediately bound exciton model for copper impurities in the bulk of ZnO proposed by Dahan et al.,<sup>72,74</sup> in which an electron component has a strong contribution from an unoccupied Cu  $d^{10}$  state. The stronger overlap between the Cu 4s state and the more delocalized hole around the impurity in our case provides the necessary stabilization of the complex by increasing the electrostatic attraction of the  $(e^-, h^+)$  pair and minimizing the electron–electron repulsion on the copper and nearest oxygen neighbors.

The interaction of a single copper atom with the VZISS is seen to follow trends in geometry and binding energy, which are commensurate with the size and charge state of the copper atom. In all three cases, copper is located approximately centrally and symmetrically between the three undercoordinated oxygen atoms of the VZISS with progressively smaller Cu–O bond distances with increasing positive charge; see Figure 6. Doubly charged copper ions are found to be most strongly bound to the VZISS with a binding energy of 24 eV, interacting both with the three undercoordinated oxygen atoms on the surface ( $\sim 1.89$  Å) and with a further undercoordinated oxygen in the second subsurface layer of oxygen atoms (2.68 Å). This latter interaction is helped by the relatively small size of the  $\text{Cu}^{2+}$  ion allowing it to be situated deep in the VZISS and enhanced

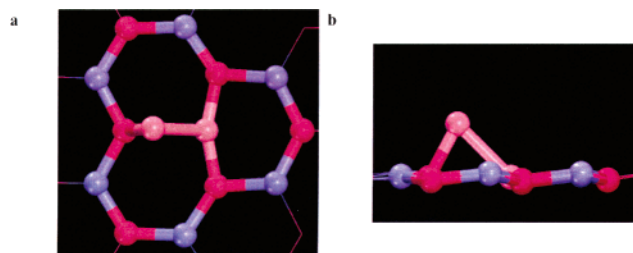


**Figure 7.** Cu dimer adsorbate in the VZISS in the oxidation state 2+: (a) top view; (b) side view.

by the electrostatic attraction of the positive copper ion to the oxygen anions. The low-lying position of the  $\text{Cu}^{2+}$  ion in the surface is suggestive of the relative ease with which  $\text{Cu}^{2+}$  ions are known to dissolve into the bulk of ZnO.<sup>1,3,6</sup> It was found crucial to include an oxygen in the second subsurface layer in the full QM region for this reason.

The singly ionized copper atom is positioned higher in the VZISS and is less strongly bound to the surface than  $\text{Cu}^{2+}$ , with a binding energy of 7.6 eV. The local structure of the  $\text{Cu}^+$  ion adsorbate is similar to a bulklike termination of the zinc surface, which is also reflected in its electronic structure. Its HOMO level is very close to the top of the valence band with the LUMO separated by about 3.8 eV that is 0.4 eV above the experimental estimate for the bottom of the conduction band. The larger size and lower charge of the  $\text{Cu}^+$  ion hinders its interaction with the second layer oxygen (3.00 Å) of the VZISS;  $\text{Cu}^+$  interacts appreciably only with the three undercoordinated surface oxygen atoms (1.99 Å). This trend is continued with the larger neutral Cu atom, which has the least affinity for the (0001)-Zn surface, bound by 2.00 eV to the surface via the three undercoordinated oxygen atoms only, with Cu–O distances ranging from 2.11 to 2.16 Å.

The HOMO of neutral copper is approximately equal to the experimental value for the bottom of the conduction band (see Figure 5). This suggests the possibility of a higher degree of hybridization of copper valence states with the surface conduction band or an overall instability of the neutral copper center by decay to a  $\text{Cu}^+$  adsorbate and a conduction electron.

**3.2. Adsorbed  $\text{Cu}_2$ .** Next, to represent the initial stages of copper cluster growth, we added a further copper atom to the single atom filled VZISS.

For the  $\text{Cu}^0$  and  $\text{Cu}^+$  filled VZISS, the interaction of the Cu adatom is mainly with the VZISS-sited copper (Cu–Cu 2.52 Å and Cu– $\text{Cu}^+$  2.48 Å) and relatively little with the surface (Cu–O 3.24–3.44 Å). Both of these species have bond lengths that are longer than their corresponding free-space neutral (2.30 Å) and singly ionized (2.45 Å) counterparts (see Table 2). The  $\text{Cu}_2^{2+}$  ion due to its deep position in the surface and its relative electron deficiency results in the Cu adatom interacting more strongly with the surface oxygen atoms forming a single Cu–O bond of 1.91 Å, with the Cu–Cu distance being 2.38 Å; see Figure 7.

Upon addition of  $\text{Cu}^0$  to the  $(\text{Cu}^+, h^+)$  complex, an electron localized on the copper ion in the VZISS leaves the 4s-like diffuse orbital and occupies a free  $3d^{10}$  state on copper, resulting in a closed shell electronic configuration for this ion, as shown by the electron deformation density plots presented in Figure 8. The driving force for this transition is the minimization of the electrostatic interactions between electrons localized on the two copper atoms as the  $3d^{10}$  state has a significantly smaller effective radius than the 4s orbital. The upper Cu species strongly bonds to one of the undercoordinated surface oxygens,

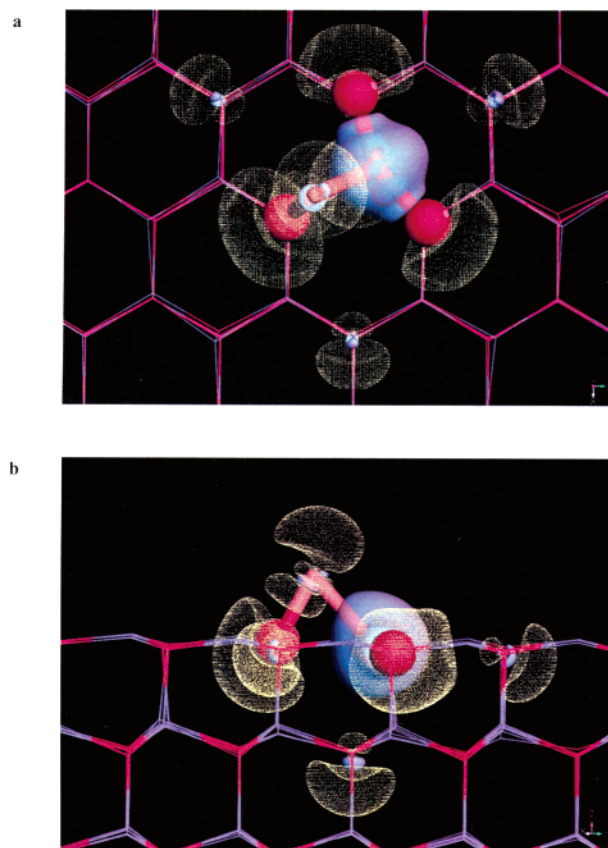


**Figure 8.** Deformation density plot, (a) top view and (b) side view, for the  $\text{Cu}^{2+}$  adsorbate. Basins with excess charge density are shown in solid and basins with the electron deficit are highlighted with dots.

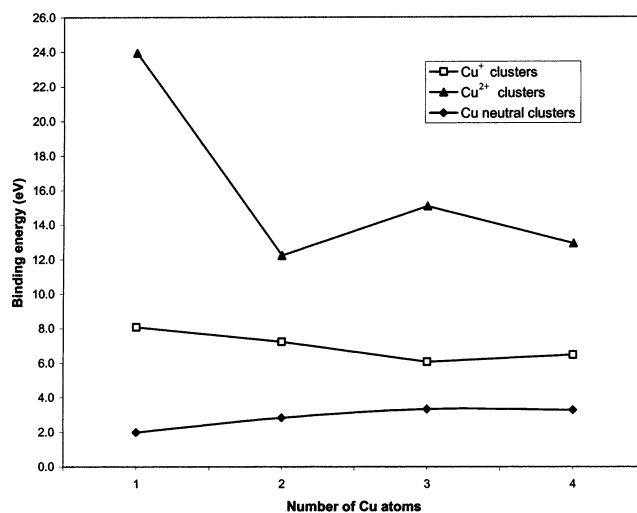


**Figure 9.** Binding energy of copper clusters with the (0001)-Zn surface with increasing cluster size. Energy defined with respect to isolated Cu clusters except for  $\text{Cu}_2^{2+}$ , see text.

thus bringing two unpaired spin states, that of  $\text{Cu}^0$  and the  $h^+$ , in close contact. The pairing of the two states leads to an overall closed shell solution.

The stabilization of the Cu–Cu bond contrasts to the free-space system where no  $\text{Cu}_2^{2+}$  dimer could be stabilized. Therefore, in this case, the  $\text{Cu}_2^{2+}$  binding energy to the ZnO surface is taken to be with respect to two separated  $\text{Cu}^+$  ions. In Figure 9, the cluster–surface binding energy is plotted for all three cluster charged states. The steep drop in binding energy between the adsorbed  $\text{Cu}^{2+}$  (23.96 eV) and the adsorbed  $\text{Cu}_2^{2+}$



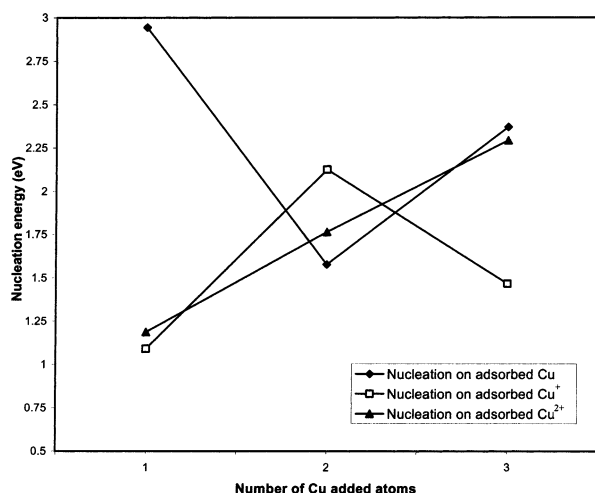


**Figure 10.** Nucleation energy of copper clusters adsorbed on the VZISS with increasing cluster size.

dimer (12.24 eV) is a result of an effective stabilization of  $\text{Cu}^{2+}$  by the surface. As seen above, on adsorption,  $\text{Cu}^{2+}$  traps an electron with an associated gain in energy, which is approximately the difference in the first and second ionization potentials of gas-phase copper. For  $\text{Cu}^+$  species, we observe a smaller decline in the binding energy between a single ion (8.09 eV) and a dimer  $\text{Cu}_2^+$  (7.24 eV). For neutral species this trend is reversed, the  $\text{Cu}_2$  dimer binds more strongly to the surface than a single atom by 0.85 eV.

Although we observe the same trend for single atom and dimer copper species in adsorption binding energies, on ZnO, through the three oxidation states, i.e.,  $E_{\text{ads}}(\text{Cu}_n^{2+}) > E_{\text{ads}}(\text{Cu}_n^+) > E_{\text{ads}}(\text{Cu}_n^0)$ , a better measure of the tendency for copper cluster growth to occur is the nucleation energy, which is defined as

$$E_{\text{nuc}} = E_{\text{ads}}(\text{Cu}_{n+1}^{(0,1+,2+)}/\text{ZnO}) - E(\text{Cu}) - E_{\text{ads}}(\text{Cu}_n^{(0,1+,2+)}/\text{ZnO}) \quad (6)$$

and gives the energy of adding an extra single copper atom to a preadsorbed copper atom or cluster. From the plot of the nucleation energy in Figure 10 we conclude that a neutral copper atom, although relatively weakly bound, provides by far the most energetically favorable adsorption site for further copper cluster growth. Considering that further copper adatoms will mainly interact with the existing copper in the VZISS, this result is unsurprising as in free space the copper dimer is the most strongly bound cluster. The unpaired 4s electron on the neutral adsorbed copper atom, favoring Cu–Cu bonding, will strongly increase the resulting nucleation energy.

**3.3. Adsorbed  $\text{Cu}_3$  Clusters.** Adding two extra copper atoms to the VZISS containing a single adsorbed copper atom leads, after optimization, to a discrete  $\text{Cu}_3$  cluster. The plane of the cluster lies perpendicular to the surface with one vertex at the approximate center of the VZISS and with two Cu–O bond distances of 2.10 Å and one shorter 2.05 Å Cu–O bond. The two other copper atoms lie vertically, almost equidistant from the surface, in the plane of the shorter Cu–O bond in the VZISS. From the copper atom in the VZISS, the two copper adatoms form Cu–Cu bond lengths of 2.43 and 2.47 Å with an angle of 62° between them. This adsorbate geometry is similar to that of a slightly “opened” acute neutral free-space  $\text{Cu}_3$  cluster, or the  $\text{Cu}_3^+$  equilateral triangular free-space cluster, but is quite unlike the lowest energy free-space obtuse  $\text{Cu}_3$  cluster; see Table 2. The increased stability provided by interaction with the

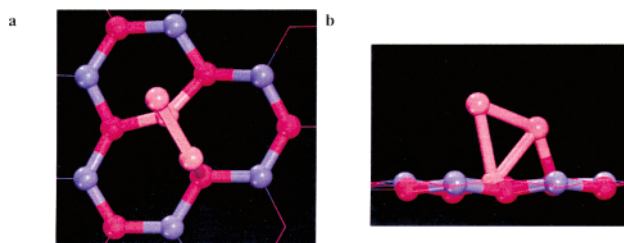


**Figure 11.** Cu trimer adsorbed on the VZISS in the oxidation state 2+.

surface accounts for the differing geometry. The obtuse angled cluster would either have an unphysically short  $\text{Zn}^{2+}$  to Cu interaction or a Cu atom that was far from the surface.

Adding two copper atoms to a singly charged Cu ion in the VZISS results in a triangular cluster tilted about an axis perpendicular to the plane of the cluster toward the surface, resulting in one copper vertex having a single Cu–O distance of 1.98 Å with an oxygen ion of the VZISS. The same oxygen ion also then “breaks” its bond with the copper in the VZISS, elongating the Cu–O bond to 2.50 Å, from 2.05 Å in the neutral case. This copper atom moves toward the other two oxygens in the VZISS, forming two equal Cu–O bonds of length 1.98 Å. The copper cluster has two approximately equal Cu–Cu bond lengths of 2.36 and 2.34 Å and one longer bond length of 2.59 Å. In contrast to the neutral adsorbed  $\text{Cu}_3$  cluster, this geometry is close to that of the ground-state neutral free-space obtuse  $\text{Cu}_3$  cluster; see Table 2.

With the addition of two copper atoms to an adsorbed  $\text{Cu}^{2+}$  ion in the VZISS, the cluster retains its bent configuration, as with the adsorbed  $\text{Cu}_3^+$ , with the corresponding vertex copper atom keeping its Cu–O bond at approximately the same length (1.97 Å); see Figure 11. The extra overall charge results in small increases in the Cu–Cu bond lengths of 0.02–0.08 Å relative to the adsorbed  $\text{Cu}_3^+$  cluster. As in the cases of  $\text{Cu}^{2+}$  and  $\text{Cu}_2^{2+}$ , the anchor in the VZISS is lower due to the stronger electrostatic interaction with the surface pulling the rest of the cluster with it. The anchor site attracts the furthest oxygen with a Cu–O separation of 2.29 Å.

The nucleation energy of adding a third adatom to form an adsorbed copper trimer is found to increase sharply for the charged clusters and decrease for the neutral cluster. The strongest stabilizing effect is the formation of a covalent bond between two  $\text{Cu}^0$  adatoms in the  $\text{Cu}_3^+$  moiety. A similar effect is observed for  $\text{Cu}_2^{2+}$ , in which a strong  $\sigma$  covalent bond is formed between the two neutral copper adatoms with a further extension of the weak covalent interaction to the diffuse  $h^+$  state, through one of the three undercoordinated surface oxygen atoms. Both charged species are further stabilized by increased interaction of adatoms with the surface oxygens as the Cu–O distances decrease, resulting in an increased shielding of the positive charge.

In contrast, the addition of an open shell Cu atom to a closed shell neutral dimer breaks the  $\sigma$  bond to create a system of delocalized 3-center bonds. On balance, this process leads to a positive nucleation energy, however, reduced in value by half from that of the first nucleation step.

**3.4. Adsorbed  $\text{Cu}_4$  Clusters.** The most stable configuration of three adatoms to a copper atom in the VZISS is a planar  $\text{Cu}_4$  cluster. The structure of the adsorbed  $\text{Cu}_4$  cluster can be simply described as an addition of a copper atom to the adsorbed neutral  $\text{Cu}_3$  cluster. The adsorbed  $\text{Cu}_3$  subcluster, within the  $\text{Cu}_4$  cluster, is almost unchanged, with the position of the copper atom in

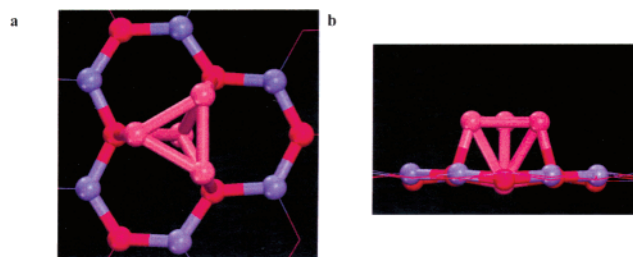


**Figure 12.** Cu tetramer adsorbed on the VZISS in the oxidation state  $2^+$ .

the VZISS and its respective Cu–O and Cu–Cu bond lengths remaining very similar. The only difference between this  $\text{Cu}_3$  subcluster and the  $\text{Cu}_3$  cluster alone, is the bond length of the upper two copper atoms, which shows a small increase from 2.44 to 2.54 Å, making the cluster triangle almost equilateral, and more significantly, the plane of orientation of the cluster is now rotated, about an axis perpendicular to the surface, to be aligned with one of the surface Zn atoms of the VZISS, and to be also slightly tilted away from this vertical axis. This change of alignment is due to the extra copper adatom, which interacts both with the  $\text{Cu}_3$  cluster and with the Zn atom of the VZISS. This copper adatom lies in the plane of the  $\text{Cu}_3$  subcluster and is bonded to one of its upper copper atoms, with a Cu–Cu bond length of 2.38 Å, and to the zinc atom in the VZISS with a Cu–Zn distance of 2.73 Å. The Cu–Zn interaction results in the zinc atom being pulled away from the surface by approximately 0.25 Å with respect to its normal relaxed position. This Cu–Zn interaction is suggestive of that described by some other authors<sup>7,9,18,19</sup> to be responsible for the creation of alloy sites that in turn have been proposed to be the active sites of Cu/ZnO catalysts for methanol synthesis.

A transition occurs from planar to three-dimensional cluster morphology for the adsorbed  $\text{Cu}_4^+$  cluster. The adsorbed  $\text{Cu}_4^+$  cluster takes the form of a slightly distorted tetrahedron and interacts with the surface via one of the Cu–Cu (2.37 Å) edges of the cluster. One of the copper atoms of this edge lies close to the center of the VZISS, slightly above the plane of the surface, interacting with two undercoordinated oxygen atoms with Cu–O bond lengths of 1.97 Å. The other copper atom of the edge lies higher above the surface and interacts both with the other undercoordinated oxygen atom of the VZISS (Cu–O 1.97 Å) and with two zinc atoms of the surface (Cu–Zn bonds of 2.80 Å and 2.73 Å). The two further copper atoms are 2.57 Å apart and lie symmetrically above the lower two copper atoms. The three-dimensional form of the cluster is in contrast to the ground-state free-space  $\text{Cu}_4^+$  cluster, which has a planar rhomboidal morphology, but is quite similar in geometry to the higher energy, metastable free-space  $\text{Cu}_4^+$  distorted tetrahedral cluster; see Table 2.

The adsorbed  $\text{Cu}_4^{2+}$  cluster, shown in Figure 12, also takes a tetrahedral form and is located symmetrically in the center of the VZISS. As for the smaller doubly charged clusters, it is lower in the VZISS relative to its neutral and single charged counterparts, with three copper adatoms lying on top of a single central copper ion. Each of the three copper adatoms interacts both with the lower central copper (similar Cu–Cu bond lengths of 2.60 Å), and with the three undercoordinated oxygen atoms (equal Cu–O bonds of 2.06 Å) of the VZISS only. The three upper copper atoms of the cluster form an equilateral triangle (Cu–Cu bond lengths of 2.40 Å) with a plane parallel to that of the surface and vertexes pointing in the direction of the lower

**TABLE 3: Energies of Adsorbed Copper Clusters on the (0001)-Zn Surface of  $\text{ZnO}^a$**

	total energy (Ha)	surface BE (eV)	HOMO (eV)	LUMO (eV)
surface	−845.56962		−5.490	0.000
$\text{Cu}/\text{ZnO}$	−2486.03228	−2.002	−2.028	−0.812
$\text{Cu}^+/\text{ZnO}$	−2485.99397	−8.541	−5.578	−1.789
$\text{Cu}^{2+}/\text{ZnO}$	−2485.87392	−25.764	−10.14	−6.434
$\text{Cu}_2/\text{ZnO}$	−4126.52957	−2.855	−3.507	−0.178
$\text{Cu}_2^+/\text{ZnO}$	−4126.42316	−7.691	−6.210	−4.183
$\text{Cu}_2^{2+}/\text{ZnO}$	−4126.30665	(−14.044)	−8.731	−6.000
$\text{Cu}_3/\text{ZnO}$	−5766.97667	−3.347	−3.208	−1.862
$\text{Cu}_3^+/\text{ZnO}$	−5766.89037	−6.525	−6.050	−3.016
$\text{Cu}_3^{2+}/\text{ZnO}$	−5766.76058	−16.893	−8.583	−6.456
$\text{Cu}_4/\text{ZnO}$	−7407.45291	−3.303	−4.102	−1.339
$\text{Cu}_4^+/\text{ZnO}$	−7407.33336	−6.932	−5.298	−3.953
$\text{Cu}_4^{2+}/\text{ZnO}$	−7407.23395	−14.730	−7.638	−4.741

<sup>a</sup> The parentheses indicate that the corresponding free-space reference state is dissociated singly charged copper ions. Surface binding energies (BE) were found with respect to clean reconstructed surface and relaxed gas-phase copper clusters.

Cu–O bonds. The adsorbed cluster is similar in geometry to the corresponding free-space  $\text{Cu}_4^+$  cluster, though having its symmetry broken by its interaction with the surface (see Table 2).

The transition from two- to three-dimensional cluster growth has in fact been experimentally reported but occurs for a 0.3 of a monolayer coverage of copper on the (0001)-Zn surface,<sup>27</sup> thus for significantly larger clusters than currently investigated.

With the adsorption of the fourth copper atom, the dependence of the binding energy of copper flattens for all species (3.30 eV for  $\text{Cu}_4$ , 6.48 eV for  $\text{Cu}_4^+$ , and 12.93 eV for  $\text{Cu}_4^{2+}$ ), with a pronounced effect only on the  $\text{Cu}_4^{2+}$ , due to a relative stabilization upon growth of the doubly ionized cluster in the gas phase. The relative invariance of the surface binding energy of the added copper atoms after the first deposition points to a relative increase in competing copper–copper cohesion within the clusters with growth. The strong monotonic increase in nucleation energy of copper adatoms on the adsorbed  $\text{Cu}_n^{2+}$  ( $n = 1–3$ ) clusters supports this argument.

From our calculations, we observe a trend of nucleation energies for  $\text{Cu}^0$  and  $\text{Cu}^+$  based clusters oscillating in anti-phase, as the pairing/unpairing of an electron on the seed cluster yields stabilization/destabilization effects, which decrease with cluster size. The linear trend for  $\text{Cu}^{2+}$  is deceptive because, although  $\text{Cu}_2^{2+}$  is a closed shell species, it does not include a strong covalent Cu–Cu bond. We suggest that on cluster growth to  $\text{Cu}_5^{2+}$  there would be a decrease in the nucleation energy with  $\text{Cu}^{2+}$  species following  $\text{Cu}^0$  cluster behavior for further nucleation.

#### 4. Electronic Structure

As shown above, by comparing the energies of the HOMOs and LUMOs of the bare (0001)-Zn surface with the corresponding levels when a VZISS is filled by copper, we can estimate the relative electronic stability of the various oxidation states of the adsorbed copper. In the following section we also assume that the system is in vacuo or a nonreactive atmosphere and consider the relative electronic stabilities within the Cu/ZnO closed system.

For adsorbed  $\text{Cu}^{2+}$  in the VZISS, the unoccupied LUMO is considerably lower than the HOMO of the bare surface (see Figure 5 and Table 3), and thus we would expect the likelihood of electron transfer from the valence band of the (0001)-Zn surface to the copper, resulting in adsorbed  $\text{Cu}^+$ . For larger

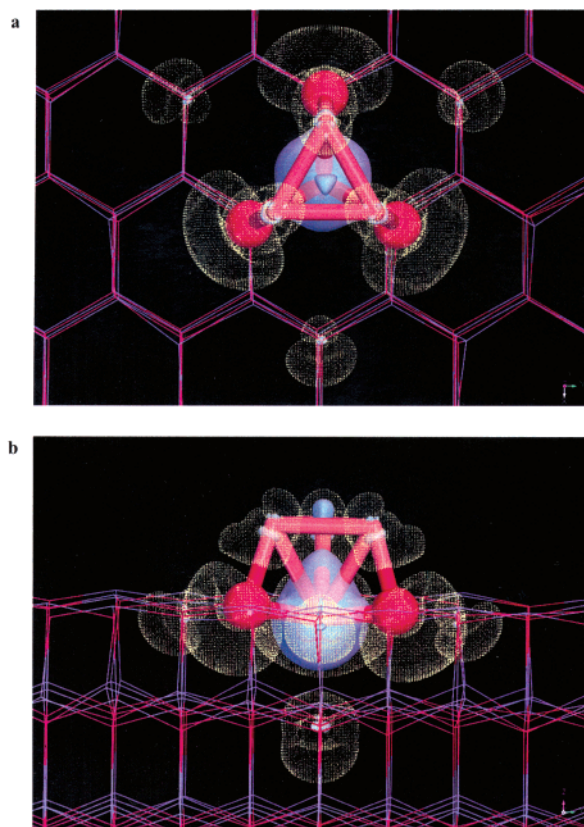


**Figure 13.** Deformation density plot (a) top view, (b) side view for the  $\text{Cu}_4^{2+}$  adsorbate. Basins with excess of charge density are shown in solid and basins with the electron deficit are highlighted with dots.

clusters, such as  $\text{Cu}_4^{2+}$ , the LUMO of the adsorbed copper system rises in energy to above that of the HOMO of the surface, indicating that larger doubly charged clusters may be stable on the (0001)-Zn surface. From Figure 13, which shows the deformation density of  $\text{Cu}_4^{2+}$ , it is clear that there is a large amount of orbital overlap between the upper copper atoms and surface oxygens, which results in back-donation from the surface to the upper three copper atoms. Overall the net charge transfer is from the surface and upper copper atoms to the lower copper in the VZISS. The integration of the deformation density shows that the hole formed by the charge transfer is shared between the surface (70%) and the upper copper atoms (30%). The lower copper in this  $\text{Cu}_4$  cluster closely resembles a  $\text{Cu}^+$  ion with a trapped electron completing the  $3d^{10}$  shell.

On cluster growth,  $\text{Cu}_4$  is the first cluster that is commensurate with the surface oxygens and therefore can stabilize an equilateral triangle cluster geometry with all three coppers of the ring having very similar local environments. However, only  $\text{Cu}_4^{2+}$  is stable in this geometry because in the other charge states, 0 or 1+, the  $\text{Cu}_3$  ring is neutral and therefore experiences electron–electron repulsion with the electron rich oxygens of the surface.

Singly charged copper, in contrast, has its LUMO well above that of the HOMO of the bare surface and thus is quite stable. Increasing the size of a singly charged adsorbed cluster to  $\text{Cu}_4^+$  lowers its LUMO but not sufficiently to cause it to be unstable to electron transfer from the surface.

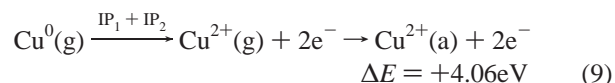
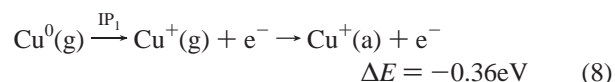
The donor states of the adsorbed neutral copper atom lie approximately at the same level as the bottom of the experimental conduction band and thus is energetically unstable to charge transfer to the surface conduction band. The acceptor

states of  $\text{Cu}^+$ , however, are also at about the same level and we would expect it to trap readily an electron from the conduction band. Therefore, for one atom adsorbed in the VZISS, we expect dynamic equilibrium between neutral and singly ionized moieties. On addition of further copper atoms, the HOMO of the cluster drops below the bottom of the experimental conduction band by 1.5 eV toward the center of the band gap. The downshift in the HOMO of neutral copper clusters breaks the dynamic equilibrium, making them deep donors. However, we envisage electron transfer from the surface of ZnO into subsurface layers, thus giving rise to an accumulation layer associated with the zinc terminated polar surface,<sup>29,75</sup> or to a  $\text{Cu}^{2+}$  moiety. Other possible, more stable, electron traps exist on the other terminating surfaces of ZnO,<sup>76,77</sup> which can be accessed by interaction with other crystallites in polycrystalline samples. Electron traps also exist as defect sites on the (0001)-Zn surface and within the ZnO bulk, acting to stabilize the donation of electrons from neutral copper.

Taking into account such possibilities, it is reasonable to suppose that at very low concentrations of copper on the (0001)-Zn surface, a mixture of Cu and  $\text{Cu}^+$  will coexist. Upon addition of further copper, the HOMO of the adsorbed copper decreases in energy, making the transition of electrons to the conduction band of ZnO progressively more unlikely, such that at higher coverages neutral copper should dominate. Experimentally, it is found that a submonolayer coverage of copper on (0001)-Zn is weakly cationic and, as the clusters become larger, neutral copper is the predominant species.<sup>27</sup>

## 5. Reaction Energies

Finally, we move from one-electron spectra to the energetics of the actual many-electron system. So far we have reported the binding energies of copper clusters on the surface, but to assess the ground state of copper clusters and the relative populations of the differently charged species, we should consider the full thermodynamic cycle. As mentioned above, copper exists as a neutral atom or an anion in the gas phase; therefore we have included the cost of ionising a copper atom in the gas phase to determine which species will be most prevalent on the ZnO surface. The binding energy must be corrected to include processes prior to adsorption, and therefore we include electron transfer from the adsorbate in the calculation of the reaction energy. For a single Cu atom we shall consider the following processes:

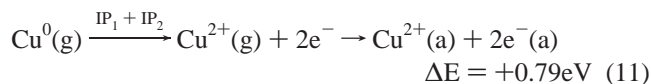
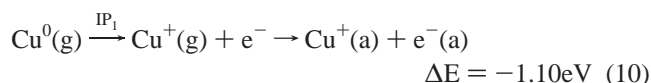


We have used experimental values for the first and second ionization potentials of a Cu atom,  $\text{IP}_1 = 7.73$  eV and  $\text{IP}_2 = 20.29$  eV, respectively,<sup>78</sup> together with a calculated adsorption energy.

Electron transfer is likely to occur on adsorption of neutral copper with electrons lost to the surface conduction band of ZnO. The binding energy of an electron,  $\text{BE}(\text{e}^-)$  in the conduction state at the zinc terminated surface has been calculated as the energy difference between the two charge states (−1 and 0) of the geometry optimized surface cluster for which



we obtain  $-0.74$  eV. Therefore two following reactions can be considered.



Following equations (7), (10), and (11), copper adsorbed in the three charged states is formed along with the electrons donated to the surface conduction band. From our calculations we can see that at the low coverage limit the dominant species on the surface will be  $\text{Cu}^0$ . However, two factors will strongly influence the ratio of  $\text{Cu}^0/\text{Cu}^+$ :

(i) Our  $\text{BE}(\text{e}^-)$  value is only the upper bound as the surface conduction states are significantly shifted up.

(ii) Charged species, as mentioned above, can be stabilized by electron transfer to hypothetical charge traps on the surface and in the bulk of ZnO, which as yet we have not fully explored. We predict significantly deeper traps in the bulk and at the oxygen terminated surface of ZnO (as also indicated by the surface band bending shown in Figure 3), which will lead to further stabilization of the charged species.

An accurate calculation of concentrations of different charge states will require improvement to the model; the extent of the overestimation of the CB and the defect formation energies should therefore determine the actual ratio of  $\text{Cu}^0/\text{Cu}^+$ .

Formation of  $\text{Cu}^{2+}$  is less favorable by 2.8 eV (which is again only an upper bound) and therefore we expect it to be present on the surface in very low concentration.

When the number of copper atoms on the surface is increased, while very low coverage is maintained, the options are whether the anchor copper is added to or the adatom is adsorbed on an adjacent VZISS. By comparison of the nucleation energy (see Figure 10) for adding a single copper to a neutral copper anchor with the reaction energy of the variously charged single copper atoms, it is clear that cluster growth is favored by ca. 1 eV. However, this process is highly exothermic and could lead to ionization of surrounding adsorbed copper clusters or self-excitation, which in turn could decay to a singly charged cluster and a conduction electron. With a significantly smaller probability there could be further ionization to  $\text{Cu}_2^{2+}$ . Despite these competing charge-transfer processes, which cannot be ignored,  $\text{Cu}_2^0$  will still dominate. As the copper clusters grow in size and the surface coverage increases, the difference in energy between  $\text{Cu}_n^{0/+2+}$  clusters converges and cluster interactions will determine the potential energy surface, which we will investigate in future studies.

## 6. Conclusions

This paper reports the first detailed study of transition metal clusters interacting with a realistic polar oxide surface. In particular, by employing a QM/MM embedding scheme, allowing for self-consistent polarization of the clusters and the oxide support, we have been able to study the interaction of copper clusters in three different oxidation states with the reconstructed polar (0001)-Zn surface of zinc oxide.

The results show that neutral copper binds strongly to the clean reconstructed polar (0001)-Zn surface, when compared to typical clean MgO surfaces for which other calculations<sup>23</sup> suggest between 25 and 50% of the adsorption energy for copper.

For higher oxidation states, the binding energy increases, with  $\text{Cu}^{2+}$  moieties binding most strongly to the (0001)-Zn surface. The latter show a tendency to adsorb relatively deeply into the surface and would be the most likely species to be absorbed into the bulk, as they have the smallest ionic radii, in agreement with the known solubility of  $\text{Cu}^{2+}$  in the bulk of ZnO. Even under the assumption of an inert or reducing atmosphere, small  $\text{Cu}^{2+}$  species are less likely to be found on the ZnO surface due to high reaction energies and its low-lying acceptor levels. Further results, however, suggest that larger  $\text{Cu}^{2+}$  clusters, when anchored to the surface by a  $(\text{Cu}^+, \text{h}^+)$  complex in a VZISS, are relatively more stable with respect to electronic transitions and reactions.

In the presence of electron traps,  $\text{Cu}^+$  ions could be energetically favored on the (0001)-Zn surface at the low coverage limit, but when the concentration of  $\text{Cu}^+$  ions increases, the electrostatic repulsion destabilizes the charged species and leads to the predominance of neutral copper. The preferred path for cluster growth is by addition of neutral copper on both  $\text{Cu}^0$  and  $\text{Cu}^+$  anchors, which explains experimental findings of weakly cationic small copper clusters on the (0001)-Zn surface in the initial stages of copper cluster growth.<sup>27</sup>

The interplay between the surface and the anchor results in stabilization of all three oxidation states of the anchor and leaving neutral copper adsorbed on top. We expect on further cluster growth two major factors will influence the morphology of the clusters: (i) the stabilizing interaction of charged copper species with available surface oxygen atoms, especially in VZISS, and that of neutral copper with terminating zinc ions, which will tend to flatten the clusters and lead to the formation of a monolayer, and (ii) the tendency for the cluster to increase the number of cohesive metal-metal bonds, which will lead to a predominance of discrete polyhedral clusters.<sup>27,79</sup> With our initial investigations reported here we provide detailed atomistic and electronic insight into the first steps of cluster growth. Calculations are currently underway examining larger copper clusters and the interplay of the two trends.

**Acknowledgment.** The development and a greater part of the application work was performed within the ESPRIT EU project QUASI, in close collaboration and with financial support from ICI/Synetix. We thank the EPSRC for provision of computer resources. We gratefully acknowledge the NWO and the British Council for financial support of this collaborative work. The molecular graphics in this paper have been produced using the Accelrys software. For useful discussions and interesting insights we are indebted to our colleagues K. Waugh, S. Cristol, L. Whitmore, J. Harding, S. Rogers, F. King, M. Watson, R. Schlögl, and L. Kantorovich.

## References and Notes

- (1) Lung-Sham, K.; Hodgson, K. O.; Solomon, E. I. *J. Am. Chem. Soc.* **1989**, *111*, 7103.
- (2) Klenov, D. O.; Kryokova, G. N.; Plyasova, L. M. *J. Mater. Chem.* **1998**, *8*, 1665.
- (3) Günter, M. M.; Ressler, T.; Jentoft, R. E.; Bems, B. *J. Catal.* **2001**, *203*, 133. Günter, M. M.; Ressler, T.; Bems, B.; Büscher, C.; Genger, T.; Hinrichsen, O.; Muhler, M.; Schlögl, R. *Catal. Lett.* **2001**, *71*, 37.
- (4) Klier, K. *Adv. Catal.* **1982**, *31*, 243.
- (5) Mehta, S.; Simmons, G. W.; Klier, K.; German, R. G. *J. Catal.* **1979**, *57*, 339.
- (6) Meitzner, G.; Inglesia, E. *Catal. Today* **1999**, *53*, 433.
- (7) Nakamura, J.; Uchijima, T.; Kanai, Y.; Fujitani, T. *Catal. Today* **1996**, *28*, 223.
- (8) Harikumar, K. R.; Rao, C. N. R. *Appl. Surf. Sci.* **1998**, *125*, 245.
- (9) Chen, H. Y.; Lau, S. P.; Chen, L.; Lin, J.; Huan, C. H. A.; Tan, K. L.; Pan, J. S. *Appl. Surf. Sci.* **1999**, *152*, 193.

- (10) Izumi, Y.; Kiyotaki, F.; Nagamori, H.; Minato, T. *J. Electron Spectrosc. Relat. Ph.* **2001**, *119*, 193.
- (11) Solomon, E. I.; Jones, P. M.; May, J. A. *Chem. Rev.* **1993**, *93*, 2623.
- (12) Kanai, Y.; Watanabe, T.; Fujitani, T.; Uchijima, T.; Nakamura, J. *Catal. Lett.* **1996**, *38*, 157.
- (13) Chinchin, G. C.; Spencer, M. S.; Waugh, K. C.; Whan, D. A. *J. Chem. Soc., Faraday Trans.* **1987**, *83*, 2193.
- (14) Pan, W. X.; Cao, R.; Roberts, D. L.; Griffin, G. L. *J. Catal.* **1988**, *114*, 440.
- (15) Ramussen, P. B.; Holmblad, P. M.; Askgaard, C. V.; Ovesen, C. V.; Stoltze, P.; Nørskov, J. K.; Chorkendorff, I. *Catal. Lett.* **1994**, *26*, 373.
- (16) Yoshihara, J.; Parker, S. C.; Schafer, A.; Campbell, C. T. *Catal. Lett.* **1995**, *31*, 513.
- (17) Topsøe, N.-Y.; Topsøe, H. *J. Mol. Catal. A: Chem.* **1999**, *141*, 95.
- (18) Clausen, B. S.; Schiøtz, J.; Gråbæk, L.; Ovesen, C. V.; Jacobsen, K. W.; Nørskov, J. K.; Topsøe, H. *Top. Catal.* **1994**, *1*, 511.
- (19) Harikumar, K. R.; Santra, A. K.; Rao, C. N. R. *Appl. Surf. Sci.* **1996**, *93*, 135.
- (20) Hu, Z.-H.; Nakatsuji, H. *Chem. Phys. Lett.* **1999**, *313*, 14.
- (21) Miyayama, M.; Hikita, K.; Uozumi, G. *Sens. Actuators B* **1995**, *25*, 383.
- (22) Thomas, J. M.; Thomas, W. J. *Principles and Practice of Heterogeneous Catalysis*; Wiley-VCH: Weinheim, 1996.
- (23) Stakheev, A. Yu.; Kustov, L. M. *Appl. Catal. A: General* **1999**, *188*, 3.
- (24) Musolino, V.; Selloni, A.; Car, R. *J. Chem. Phys.* **1998**, *108*, 5044.
- (25) Musolino, V.; Dal Corso, A.; Selloni, A. *Phys. Rev. Lett.* **1999**, *83*, 2761.
- (26) Lopez, N.; Illas, F.; Röscher, N.; Pacchioni, G. *J. Chem. Phys.* **1999**, *110*, 4873.
- (27) Lopez, N.; Illas, F. *J. Mol. Catal. A: Chem.* **1997**, *119*, 177.
- (28) Yudannov, I.; Pacchioni, G.; Neyman, K.; Röscher, N. *J. Phys. Chem. B* **1997**, *101*, 2786.
- (29) Lopez, N.; Pacchioni, G.; Maseras, F.; Illas, F. *Chem. Phys. Lett.* **1998**, *294*, 611.
- (30) Lopez, N.; Illas, F.; Pacchioni, G. *J. Am. Chem. Soc.* **1999**, *121*, 813.
- (31) Lopez, N.; Illas, F.; Pacchioni, G. *J. Phys. Chem. B* **1999**, *103*, 1712.
- (32) Komolov, S. A.; Lazneva, E. F.; Egebjerg, T.; Møller, P. J. *J. Phys.: Condens. Matter* **1997**, *9*, 7297.
- (33) Yoshihara, J.; Campbell, J. M.; Campbell, C. T. *Surf. Sci.* **1998**, *406*, 235.
- (34) Yoshihara, J.; Parker, S. C.; Campbell, C. T. *Surf. Sci.* **1999**, *439*, 153.
- (35) Harikumar, K. R.; Santra, A. K. *Solid State Commun.* **1996**, *99*, 403.
- (36) Henrich, V. E.; Cox, P. A. *The surface science of Metal Oxides*; Cambridge University Press: Cambridge, U.K., 1996.
- (37) Bowker, M.; Houghton, H.; Waugh, K. C. *J. Chem. Soc., Faraday Trans. 1* **1981**, *77*, 3023.
- (38) French, S. A.; Sokol, A. A.; Bromley, S. T.; Catlow, C. R. A.; Rogers, S. C.; King, F.; Sherwood, P. *Angew. Chem., Int. Ed.* **2001**, *113*, 4569.
- (39) Tasker, P. W.; Stoneham, A. M. *Mater. Res. Soc. Symp. Proc.* **1985**, *40*, 291.
- (40) Stefanovich, E. V.; Truong, T. N. *J. Chem. Phys.* **1995**, *102*, 5071.
- (41) Kantorovich, L. N.; Shluger, A. L.; Sushko, P. V.; Stoneham, A. M. *Surf. Sci.* **2000**, *444*, 31.
- (42) Nygren, M. A.; Pettersson, L.; Freitag, A.; Staemmler, V.; Gay, D. H.; Rohl, A. L. *J. Phys. Chem.* **1996**, *100*, 294.
- (43) Pacchioni, G.; Ferrari, A. M.; Marquez, A. M.; Illas, F. *J. Comput. Chem.* **1997**, *18*, 617.
- (44) Schneider, W. F.; Hass, K. C.; Miletic, M.; Gland, J. L. *J. Phys. Chem. B* **2002**, *106*, 7405.
- (45) Grey, T.; Gale, J.; Nicholson, D.; Artacho, E.; Soler, J. *Stud. Surf. Sci. Catal.* **2000**, *128*, 89.
- (46) Read, M. S. D.; Islam, S. M.; King, F.; Hancock, F. E. *J. Phys. Chem. B* **1999**, *103*, 1558.
- (47) Whitmore, L.; Sokol, A. A.; Catlow, C. R. A. *Surf. Sci.* **2002**, *498*, 135.
- (48) Antes, I.; Thiel, W. *J. Phys. Chem. A* **1999**, *103*, 9290.
- (49) Sierka, M.; Sauer, J. *Faraday Discuss.* **1997**, *106*, 41.
- (50) Svensson, M.; Humbel, S.; Froese, R. D. J.; Matsubara, T.; Sieber, S.; Mokomura, K. *J. Phys. Chem.* **1996**, *100*, 19357.
- (51) Hay, P. J.; Wadt, W. R. *J. Chem. Phys.* **1985**, *82*, 270, 284, 299.
- (52) Dolg, M.; Wedig, U.; Stoll, H.; Preuss, H. *J. Chem. Phys.* **1987**, *86*, 866.
- (53) Dick, B. G.; Overhauser, A. *Phys. Rev.* **1958**, *112*, 90.
- (54) Sherwood, P.; Vries, A. H. de; Collins, S. J.; Greatbanks, S. P.; Burton, N. A.; Vincent, M. A.; Hillier, I. H. *Faraday Discuss.* **1997**, *106*, 79.
- (55) Gale, J. D. *J. Chem. Soc., Faraday Trans.* **1997**, *93*, 629.
- (56) Guest, M. F.; Lenthe, J. H. van; Kendrick, J.; Schoffel, K.; Sherwood, P. with contributions from Amos, R. D.; Bunker, R. J.; Dam, H. J. J. van; Dupuis, M.; Handy, N. C.; Hillier, I. H.; Knowles, P. J.; Bonacic-Koutecky, V.; Niessen, W. von; Harrison, R. J.; Rendell, A. P.; Saunders, V. R.; Stone, A. J.; Tozer, D. J.; Vries, A. H. de. GAMESS-UK, a package of ab initio programs. The package is derived from the original GAMESS code due to M. Dupuis, D. Spangler, and J. Wendoloski, NRCC Software Catalog, Vol. 1, Program No. QG01 (GAMESS), 1980.
- (57) Lewis, G. V.; Catlow, C. R. A. *J. Phys. C: Solid State Phys.* **1985**, *18*, 1149.
- (58) Binks, D. J.; Grimes, R. W. *J. Am. Ceram. Soc.* **1993**, *76*, 2730.
- (59) Nyberg, M.; Nygren, M. A.; Petersson, L. G. M.; Gay, D. H.; Rohl, A. L. *J. Phys. Chem.* **1996**, *100*, 9054.
- (60) Tasker, P. W. *J. Phys. C* **1979**, *12*, 4977.
- (61) Noguera, C. *J. Phys. Condens. Matter* **2000**, *12*, R367.
- (62) Jedrecy, N.; Sauvage-Simkin, M.; Pinchaux, R. *Appl. Surf. Sci.* **2000**, *162*, 69.
- (63) Dulub, O.; Boatner, L. A.; Diebold, U. *Surf. Sci.* **2002**, *519*, 201.
- (64) Dulub, O.; Diebold, U.; Kresse, G. *Phys. Rev. Lett.* **2003**, *90*, 016102-1.
- (65) Kunat, M.; Girol, S. G.; Becker, T.; Burghaus, U.; Wöll, C. *Phys. Rev. B* **2002**, *66*, 081402.
- (66) French, S. A.; Sokol, A. A.; Bromley, S. T.; Catlow, C. R. A.; Rogers, S. C.; Sherwood, P. *J. Chem. Phys.* **2003**, *118*, 317.
- (67) Gay, D. H.; Rohl, A. L. *J. Chem. Soc., Faraday Trans.* **1997**, *93*, 629.
- (68) Young, K. F.; Frederikse, H. P. R. *J. Phys. Chem. Ref. Data* **1973**, *2*, 313.
- (69) Vosko, S. H.; Wilk, L.; Nusair, M. *Can. J. Phys.* **1980**, *58*, 1200.
- (70) Becke, A. D. *J. Chem. Phys.* **1993**, *98*, 5648.
- (71) Becke, A. D. *J. Chem. Phys.* **1997**, *107*, 8554.
- (72) Hamprecht, F. H.; Cohen, A. J.; Tozer, D. J.; Handy, N. C. *J. Chem. Phys.* **1998**, *109*, 6264.
- (73) Schäfer, A.; Horn, H.; Ahlrichs, R. *J. Chem. Phys.* **1992**, *97*, 2571.
- (74) Schäfer, A.; Huber, C.; Ahlrichs, R. *J. Chem. Phys.* **1994**, *100*, 5829.
- (75) Åslund, N.; Barrow, R. F.; Richards, W. G.; Travis, D. N. *Ark. Fys.* **1965**, *30*, 171.
- (76) Morse, M. D. *Chem. Rev.* **1986**, *86*, 1049.
- (77) McCaffrey, J. G.; Bennett, R. R.; Morse, M. D.; Breckenridge, W. H. *J. Chem. Phys.* **1989**, *91*, 92.
- (78) Balbuena, P. B.; Derosa, P. A.; Seminario, J. M. *J. Phys. Chem. B* **1999**, *103*, 2830.
- (79) Calaminici, P.; Koster, A. M.; Russo, N.; Salahub, D. R. *J. Chem. Phys.* **1996**, *105*, 9546.
- (80) Langhoff, S. R.; Bauschlicher, C. W., Jr.; Walch, S. P.; Laskowski, B. C. *J. Chem. Phys.* **1996**, *85*, 7211.
- (81) Faas, S.; Snijders, J. G.; Lenthe, J. H. van; Lenthe, E. van; Baerends, E. *J. Chem. Phys. Lett.* **1995**, *246*, 632.
- (82) Dahan, P.; Fleurov, V.; Thurian, P.; Heitz, R.; Hoffmann, A.; Broser, I. *Phys. Rev. B* **1998**, *57*, 9690.
- (83) Fons, P.; Nakahara, K.; Yamada, A.; Iwata, K.; Matsubara, K.; Takasu, H.; Niki, S. *Phys. Stat. Solidi B* **2002**, *229*, 849.
- (84) Dahan, P.; Fleurov, V.; Thurian, P.; Heitz, R.; Hoffmann, A.; Broser, I. *J. Phys.: Condens. Matter* **1998**, *10*, 2007.
- (85) Kronik, L.; Shapira, Y. *Surf. Sci. Rep.* **1999**, *37*, 1.
- (86) González-Elipe, A. R.; Soria, J. J. *J. Chem. Soc., Faraday Trans. 1* **1988**, *84*, 3961.
- (87) Yu, B.; Zhu, C.; Gan, F.; Huang, Y. *Mater. Lett.* **1998**, *33*, 247.
- (88) Lide, D. R., Ed. *CRC Handbook of Chemistry and Physics*; CRC Press: London, 2002.
- (89) Didziulis, S. V.; Butcher, K. D.; Cohen, S. L.; Solomon, E. I. *J. Am. Chem. Soc.* **1989**, *111*, 7110.
- (90) Bulk calculations have been performed using the same hybrid QM/MM embedded cluster approach as described in section 2. The QM cluster has been centered on a zinc site and includes 39 atoms, in three parallel ZnO layers, composed of 13 atom island-like fragments, details of these calculations will be reported elsewhere.